Journal of Alloys and Compounds 1075 (2026) 189252

Contents lists available at ScienceDirect

Journal of Alloys and Compounds

journal homepage: www.elsevier.com/locate/jalcom

Thermally stabilized NiFeS nanowire electrodes for long-term alkaline oxygen evolution

Salvatore Geraci [a], Roberto Luigi Oliveri [a], Bernardo Patella [a], Nadia Moukri [a], Filippo Pellitteri [a], Rosario Miceli [a], Priyadharshini Matheswaran [b], Philippe Mandin [b], Myeongsub Kim [c], Rosalinda Inguanta [a,*]

[a] Department of Engineering, Università degli Studi di Palermo, Viale delle Scienze, Palermo 90128, Italy
[b] Institut de Recherche Dupuy de Lôme, UMR CNRS 6027, Lorient 56100, France
[c] Department of Ocean and Mechanical Engineering, Department of Biomedical Engineering, Florida Atlantic University, Boca Raton, USA

ARTICLE INFO

Keywords:
NiFeS nanowires
Oxygen evolution reaction
Alkaline water electrolysis
Intermittent power supply
Thermal treatment
Electrocatalyst stability

ABSTRACT

The development of durable and highly active electrocatalysts is essential for advancing cost-effective hydrogen production through alkaline water electrolysis. In this work, we report template-assisted electrodeposition of composition-optimized NiFeS nanowires, followed by a low-temperature thermal treatment designed to stabilize sulphur species and improve durability. The resulting ternary alloy, containing 17 at% sulphur and 7 at% iron, exhibited remarkable oxygen evolution activity, which may be related to its partially amorphous nature and the sulphur-induced increase in active site density. However, medium- and long-term stability tests revealed progressive sulphur leaching and a consequent loss of the catalytic performance in the untreated samples. To mitigate this effect, post-deposition thermal treatment was introduced. After thermal treatment, the NiFeS nanowires required an overpotential of 206 mV at a current density of 10 mA cm^{-2} and exhibited fast reaction kinetics with a Tafel slope of 30 mV dec^{-1} in 30 wt% KOH. Long-term electrolysis experiments showed only a 30 mV increase in operating potential after 125 h of continuous operation at ambient temperature, indicating improved durability. Structural and compositional characterization confirmed that heat treatment effectively suppresses sulphur loss while preserving electrode integrity. Overall, these results demonstrate that thermally treated NiFeS nanostructured electrodes are highly promising oxygen evolution catalysts for alkaline electrolysis, offering a practical route to combine excellent catalytic performance with prolonged operational stability.

1. Introduction

Climate change represents one of the most pressing global challenges of the present century; reducing greenhouse gas emissions is a fundamental priority for limiting global temperature rise [1]. Within this framework, the move toward sustainable energy systems has markedly intensified in recent years, driving a swift rollout of renewable technologies, including solar and wind power. Nonetheless, the fluctuating output of these resources makes the development of effective energy storage and management solutions indispensable [2,3].

Hydrogen is an attractive energy carrier because it enables the storage of surplus renewable electricity and its later conversion into power or fuels. Among the different hydrogen production routes, electrolytic water splitting powered by renewable electricity provides an environmentally friendly and viable pathway for industrial-scale hydrogen production [4,5]. However, the relatively high production cost of hydrogen produced by electrolysis remains a major challenge compared to hydrogen derived from fossil-based processes. Accordingly, ongoing intensive research is targeting enhancements in electrolyzer efficiency alongside reductions in their operating expenses [6,7].

Among the available electrolysis systems, alkaline water electrolyzers (AEs) are considered one of the most mature and commercially established technologies for hydrogen production [8]. In contrast to proton exchange membrane (PEM) electrolyzers, which rely on platinum-group electrocatalysts, alkaline systems can operate with catalysts based on abundant and inexpensive transition metals. These features make alkaline electrolysis particularly attractive for the large-scale implementation of green hydrogen production. Accordingly, current

* Corresponding author.
E-mail address: rosalinda.inguanta@unipa.it (R. Inguanta).

https://doi.org/10.1016/j.jallcom.2026.189252
Received 25 March 2026; Received in revised form 12 June 2026; Accepted 14 June 2026
Available online 15 June 2026

studies thus prioritize the optimization of electrode materials to boost electrocatalytic performance and cut energy losses during operation [9,10].

In alkaline water electrolysis, the oxygen evolution reaction (OER) is widely regarded as the slowest step of the process, and therefore, a key factor determines the energy efficiency of the system. The sluggish kinetics arise from the complex multistep mechanism involving four-electron and proton transfers necessary to form the oxygen–oxygen bond. Overcoming the kinetic barriers associated with OER is therefore essential to lowering the overall energy consumption and enhancing the efficiency of water-splitting systems, especially in alkaline electrolyzers, where the activation of this reaction remains particularly challenging [11,12].

Ni-based alloys rank among the most widely used electrocatalysts for alkaline electrolysis, owing to their excellent chemical resilience in harsh alkaline media and superior electrical conductivity [13]. Compared with noble metals, nickel offers an attractive compromise between cost and performance, making it particularly attractive for water electrolysis [14]. Incorporating iron into nickel-based structures enhances OER electrocatalysis by lowering the required overpotential, so Ni-Fe alloys are considered highly promising for improving electrolyzer efficiency without significantly increasing costs. Iron improves electronic conductivity and electrode stability, facilitating charge transfer and reducing energy losses [15,16]. However, the relatively low intrinsic electrical conductivity of many Ni–Fe (oxy)hydroxide phases remains a drawback. To address this challenge, extensive research has focused on engineering NiFe oxides and hydroxides through nanostructuring [17], surface atom incorporation [18,19], and hybridization with conductive matrices [20].

The introduction of a third element, such as sulphur, can further improve electrode performance. Recent studies on nickel–iron-based nanosheet electrocatalysts have shown that sulphur incorporation can enhance conductivity and OER activity [21,22]. By tuning the alloy electronic properties, sulphur increases the population of catalytically active sites and facilitates charge transfer, thereby lowering the overpotentials of key electrochemical processes and improving overall electrolyzer performance. In addition, nickel–iron–sulphur alloys often exhibit an amorphous structure, and this atomic disorder can contribute to greater chemical stability and a more homogeneous distribution of active elements. As a result, electrode durability is improved, and structural degradation processes that typically limit the lifetime of conventional electrodes are mitigated [23,24].

Nevertheless, conventional NiFeS catalysts are typically produced via multi-step processes such as oxidation/sulfidation, sintering-aided deposition, or hydrothermal synthesis, which often lead to inhomogeneous active phase distribution and weak substrate binding. Furthermore, nanoparticulate catalysts can hinder mass transport at high current densities, thereby limiting their practical applicability. In addition, autoxidation processes, which are almost unavoidable under anodic operation, may decrease conductivity and cause dissolution of active species over time [25,26].

In this work, a template-assisted pulsed electrodeposition strategy is employed to fabricate three-dimensional (3D) nickel–iron–sulphide nanowires (NiFeS NWs) with controlled composition and morphology, followed by a low-temperature thermal treatment aimed at stabilizing sulphur species and enhancing durability under OER conditions [27]. Compared with conventional planar electrodes, the nanowire architecture provides a high density of accessible active sites, efficient charge-transport pathways, and strong adhesion to the nickel substrate, thereby supporting stable operation under prolonged electrochemical polarization. The incorporation of sulphur into the Ni–Fe framework promotes electronic modulation and may contribute to the formation of defect-rich surfaces that are beneficial for OER catalysis. Importantly, the present study focuses on the combined advantages of composition control, nanostructuring, sulphur stabilization, and practical validation in alkaline electrolyzer conditions. This integrated approach is intended to address both catalytic activity and operational durability, which are essential requirements for real-device applications [28–30].

To investigate the sulphur role in the alloy, the S content was varied during electrodeposition. The starting point of this work is the best-performing NiFe alloy electrode of the previous study [31]. Structural and compositional analyses confirmed that heat treatment reduces sulphur loss and preserves electrode integrity, highlighting NiFeS nanostructured electrodes as promising candidates for alkaline electrolysis. These results demonstrate that thermal treatment is an effective strategy to achieve both high catalytic performance and improved long-term operational stability. In addition, the simulation results for coupling an alkaline electrolyzer with NiFeS nanostructured electrodes to a photovoltaic system are reported. The performance of a laboratory-scale alkaline electrolysis cell equipped with the developed nanostructured electrodes was also evaluated.

2. Material and methods

Nickel–iron–sulphur (NiFeS) nanostructured electrodes were fabricated by template electrodeposition, a straightforward and cost-effective method carried out at ambient temperature under atmospheric pressure. This fabrication procedure is described in detail elsewhere [31]. This technique enables the deposition of the desired material onto a conductive substrate, while the final morphology of the electrodes is primarily determined by the type of template used. We utilized a Whatman polycarbonate membrane featuring $\sim 10^{12}$ pores per m^2, pore diameters of 220–250 nm, and 20 μm thickness. Its porous structure directs the electrodeposition of aligned cylindrical nanowires (NWs).

Before electrodeposition, the membrane was made conductive by depositing a thin gold layer by sputtering on one side. The coating was performed using a Quorum T300 Plus multitarget sputter coater under a continuous current of 120 mA until a gold layer of 30 nm was achieved. Next, a dense nickel film was electrochemically deposited on the Au-sputtered membrane surface. This layer ensured mechanical integrity and served as a current collector linking all embedded nanowires. Deposition occurred in a standard Watts bath (300 g L^{-1} $NiSO_4 \cdot 6H_2O$, 45 g L^{-1} $NiCl_2 \cdot 6H_2O$, and 45 g L^{-1} H_3BO_3) using a three-electrode cell (Au-coated membrane as working electrode, Pt counter electrode, and saturated calomel reference (SCE) via potentiostatic mode at −1.15 V vs. SCE for 2.5 h (current-time transient in Fig. S1).

After the formation of the nickel current collector, the nanowires were deposited. The electrolyte for NW fabrication consisted of the Watt's bath supplemented with 0.44 M $FeSO_4 \cdot 7H_2O$ (selected based on previous experimental work) and different concentrations of $Na_2S_2O_3 \cdot 5H_2O$ (5, 10, and 15 g L^{-1}). At this stage, the pH of the solution was about 3 and was adjusted to 4.25 by adding 0.1 M NaOH before deposition. The NiFeS NWs were obtained by pulsed electrodeposition using a square-wave potential profile, cycling the potential between −0.55 V and −1.05 V vs. SCE for a total of 80 cycles. The upper and lower potentials were applied for 4 s and 6 s, respectively. Fig. S1 further displays representative voltage and current density transients from the NW electrodeposition.

The final step of the fabrication process was template removal, achieved by dissolving the polycarbonate membrane in four consecutive 5 min baths of pure chloroform. During dissolution, a large portion of the sputtered gold is removed together with the template. In particular, the thin gold coating on the non-porous areas is eliminated, while only the gold located between the nanowire base and the Ni current collector is retained. After template removal, the resulting NiFeS NW electrodes were subjected to thermal treatment in a tubular Lenton TSH15 furnace under a nitrogen atmosphere. The temperature ramped from ambient to the target at 20 °C min^{-1} , dwelled for 3 min, then passively cooled to ambient temperature. In this study, heat treatment was carried out from 150 °C to 500°C. These values were selected considering the data reported in [10,32].

Before electrochemical performance evaluation, electrode morphology and elemental composition were probed via field-emission gun scanning electron microscopy (FEG-SEM; FEI Quanta 200) coupled with energy-dispersive X-ray spectroscopy (EDS). To validate the data obtained from EDS, inductively coupled plasma optical emission spectroscopy (ICP-OES; PerkinElmer Avio 220 Max) was performed, providing a more accurate determination of the elemental composition. Standard solutions of Ni, Fe and S were first used to generate calibration plots. The alloy nanowires were then separated from the substrate and fully decomposed in aqua regia prepared with nitric acid and hydrochloric acid in a 1:3 vol ratio. The resulting solution was subsequently diluted with Milli-Q water.

Crystal phases were identified by X-ray diffraction (XRD; Rigaku D-Max 25600 HK diffractometer, 5°–80° 2θ range). Surface oxidation states were examined by X-ray photoelectron spectroscopy (XPS) using a PHI5000 VersaProbe II system (ULVAC-PHI, Chigasaki, Japan) equipped with a monochromatic Al Kα source (1486.6 eV). Measurements were performed with a 100 μm beam size, 25 W power, and at an incident angle of 45°. Spectra were collected in FAT mode with a pass energy of 23.5 eV, and charge compensation was applied using a dual electron and Ar^+ ion neutralization. Each spectral region was acquired for 20 min, and the data were processed with MultiPak software (version 9.9.3, ULVAC-PHI). Raman spectroscopy measurements were carried out using a micro-Raman (Renishaw inVia Raman Microscope) to further investigate the structural features of the samples. Tests were performed using the 633 nm laser at 50X.

Performance was assessed at ambient temperature in 30 wt% KOH using a three-electrode cell: NiFeS NWs (geometric area 0.6 cm^2) as working electrode, Ni foil counter electrode, and Hg/HgO (0.1 M) reference (in the text, all potential values were converted to reversible hydrogen electrode, RHE, scale). The reference electrodes were periodically cleaned, refilled with a fresh solution of 0.1 M KOH, and calibrated using a new reference electrode that was not used for the electrochemical tests. All electrochemical measurements were repeated at least three times to ensure reproducibility and reliability of the collected data.

3. Results and discussion

Arrays of NiFeS nanowires with different compositions were obtained by varying the sodium thiosulfate concentration in the electrodeposition bath. Fig. 1a shows a representative top-view SEM image of the NiFeS NW electrodes prepared with 15 g L^{-1} of $Na_2S_2O_3$. The nanowires displayed a well-defined cylindrical morphology and uniform spacing. Typical interconnections between adjacent NWs, arising from pore coalescence in the template, were also clearly visible. NWs formed a uniform coating on the current collector, with diameters ranging from 220 to 250 nm and lengths of approximately 10–11 μm. As anticipated, the morphology remained independent of the alloy composition and was determined solely by the template geometry. Fig. 1b shows the same sample after thermal treatment at 150 °C. At this temperature, as well as at the other investigated temperatures, the NW structure did not change during annealing, suggesting good mechanical stability of the nanostructures. Figs. 1c and 1d show the cross-sectional SEM images of the same samples, confirming the uniform coverage of the nickel current collector by firmly anchored NWs.

The effect of sodium thiosulfate concentration in the deposition bath on the performance of the NiFeS ternary alloy was investigated. Fig. 2 shows the EDS spectra of samples prepared with 5, 10, and 15 g L^{-1} $Na_2S_2O_3$, compared to the best-performing NiFe binary alloy

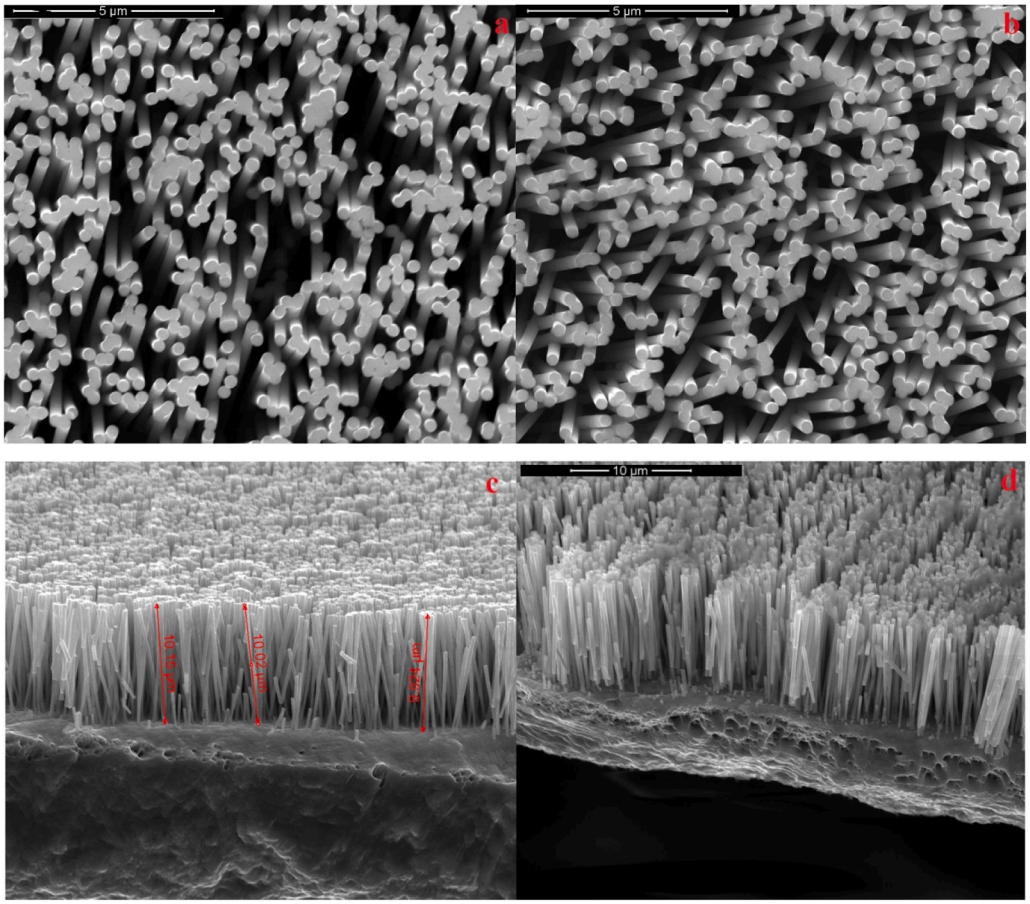

Fig. 1. Top-view SEM images of a) NiFeS NWs b) NiFeS HT_{150} and c-d) cross-section.

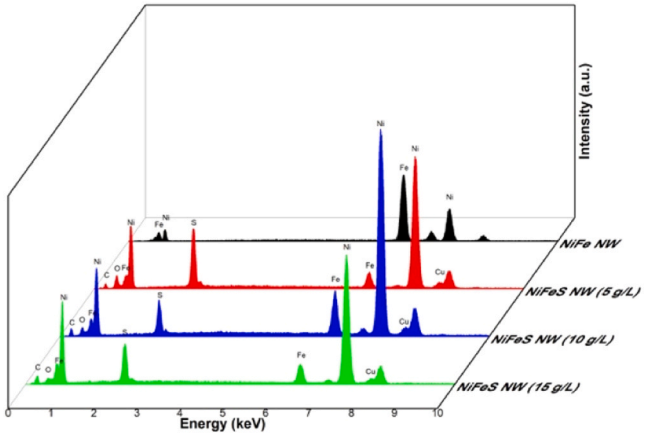

Fig. 2. EDS spectra of different NWs electrodes: black) NiFe NW; red) NiFeS NW 5 g/L; blue) NiFeS NW 10 g/L; red) NiFeS NW 15 g/L.

obtained from the same bath without thiosulfate. EDS analyses were performed on NWs detached from the electrode surface using carbon tape to avoid interference from the nickel current collector.

The compositions of the alloys differed markedly (Table 1). The binary NiFe alloy was Fe-rich (78 at% Fe), in agreement with literature data [33,34]. To validate the compositional analysis obtained by EDS, inductively coupled plasma optical emission spectroscopy (ICP-OES) was performed. In particular, the NWs were detached from the current collector and dissolved in aqua regia. The corresponding solution was then diluted in ultrapure water and analysed after the calibration for the three elements. A detailed comparison between the atomic percentages obtained by EDS and ICP-OES is reported in Table S1. Despite the intrinsic differences between the two analytical techniques, a good agreement was observed for Ni, Fe, and S contents in all samples, confirming the reliability of the EDS measurements and the representativeness of the elemental compositions reported in Table 1.

The NiFeS HT_{150} sample exhibited only minor compositional variations after thermal treatment, indicating that annealing at 150 °C does not significantly alter the overall alloy composition.

The deposition of NiFe follows the "anomalous co-deposition" mechanism, which is characterized by the preferential deposition of the less noble metal (Fe) compared to the more noble one (Ni) [35]. Several mechanisms have been proposed to explain this behaviour [36,37]. The most plausible explanation, proposed by Matlosz [37] describes the adsorption of Fe intermediate species on the electrode surface despite ongoing Ni deposition. In nanochannels, this surface blocking effect is enhanced, resulting in Fe-rich NWs [38,39]. As shown by Llavona et al. [38], is particularly pronounced in nanoporous templates. The presence of sodium thiosulfate and the pH adjustment (from 3 to 4.25) profoundly altered the deposition mechanism and alloy composition. Thiosulfate ($S_2O_3^{2-}$) is reduced through a series of reactions, yielding metal sulphides (NiS, FeS) and amorphous sulphur embedded in the deposit [23,40]. At moderately acidic pH (~4.25), thiosulfate is relatively stable but undergoes partial decomposition, releasing sulphide ions that react with deposited metal cations [41]. This results in a mixed microstructure comprising crystalline and amorphous regions [42]. Nickel is mainly deposited in metallic form, while iron may be present as metal or amorphous sulphide inclusions. The resulting low-crystallinity structure is advantageous for electrocatalytic applications. Increasing the thiosulfate concentration had little effect on the Ni content but strongly influenced the Fe and S contents.

Table 1
Composition of NiFeS and NiFe NWs determined by EDS analysis (SD 2%).

Element (at %)	NiFeS 5 g/L	NiFeS 10 g/L	NiFeS 15 g/L	NiFe	NiFeS HT_{150}
Ni	73.00	79.34	76.1	22	76.5
Fe	16.18	9.46	6.8	78	6.77
S	10.82	11.2	17.1	-	16.73

Fig. 3 shows the XRD patterns of the NiFeS NW electrodes. All NiFeS samples exhibited similar diffraction patterns, with peaks at 44.53°, 51.86°, and 76.37° attributable to the face-centered cubic α-Ni structure [PDF card no. 04–850], corresponding to the (111), (200), and (220) planes. A gold peak from the sputtering seed layer was observed at 38.21°. Only Ni peaks were detected, as they arise from both the current collector and the metallic Ni phase in the NWs. As reported in [23], sulphur-containing phases were amorphous and therefore undetectable by XRD. However, the presence of amorphous sulphide inclusions led to an increase (0.379° for 5 g L−1 and 0.491° for 15 g L−1in the mean half-width of the main peak located at 44.44°. Heat treatment at 150 °C did not alter the XRD pattern (the mean half-width of the main peak for the sample obtained with 15 g L−1 is 0.484), confirming preservation of the amorphous structure.

X-ray photoelectron spectroscopy (XPS) was used to investigate the surface chemical states of the samples. The high-resolution Ni 2p, Fe 2p, and S 2p spectra of NiFeS NW are shown in Fig. 4a–c. The Ni $2p_{3/2}$ region (Fig. 4a) is dominated by a broad multiplet centered at approximately 855 eV, with satellite features at higher binding energies (~861–866 eV), consistent with oxidized Ni species. This indicates that nickel at the surface is primarily present in an oxidized state rather than as metallic Ni⁰ (which is expected at ~852.6 eV), in agreement with previous reports [43–46].

The Fe $2p_{3/2}$ spectrum (Fig. 4b) shows a multiplet centered at around 712 eV, characteristic of Fe^{3+} species, with a minor contribution at lower binding energy (~706.6 eV) that may be attributed to a small amount of metallic Fe. The S 2p spectrum (Fig. 4c) exhibits a doublet in the low binding energy region (~162–164 eV), assigned to sulphide species, together with additional components at higher binding energies (~168–170 eV), associated with oxidized sulphur species such as sulphates or thiosulfates. These features indicate that partial surface oxidation of sulphur is present in the as-prepared material [45,47].

After thermal treatment at 150°C (NiFeS HT150), the corresponding Ni 2p, Fe 2p, and S 2p spectra (Fig. 4d–f) show that the most evident changes occur in the sulphur region, whereas the Ni and Fe signals remain largely unchanged. The Ni 2p spectrum (Fig. 4d) retains a similar multiplet structure and binding energy positions, suggesting that the Ni chemical state is essentially preserved. Likewise, the Fe 2p spectrum (Fig. 4e) does not show significant shifts or changes in spectral shape, indicating that Fe remains predominantly oxidized. In contrast, the S 2p

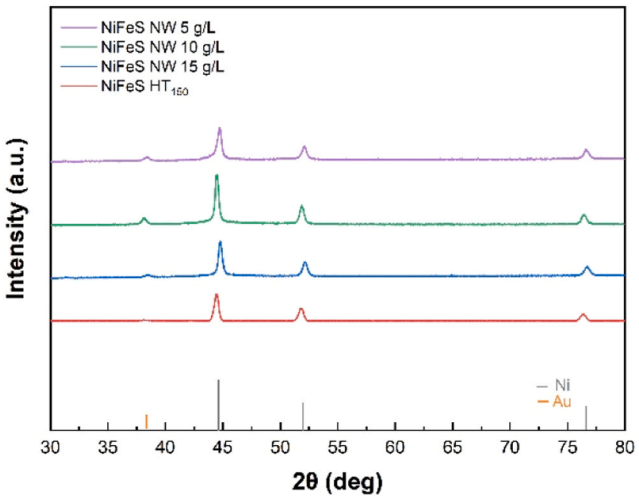

Fig. 3. XRD patterns of NiFeS NWs electrodes prepared at different $Na_2S_2O_3$ concentrations: purple) 5 g/L; green) 10 g/L; blue) 15 g/L; red) 15 g/L after heat treatment at 150°C.

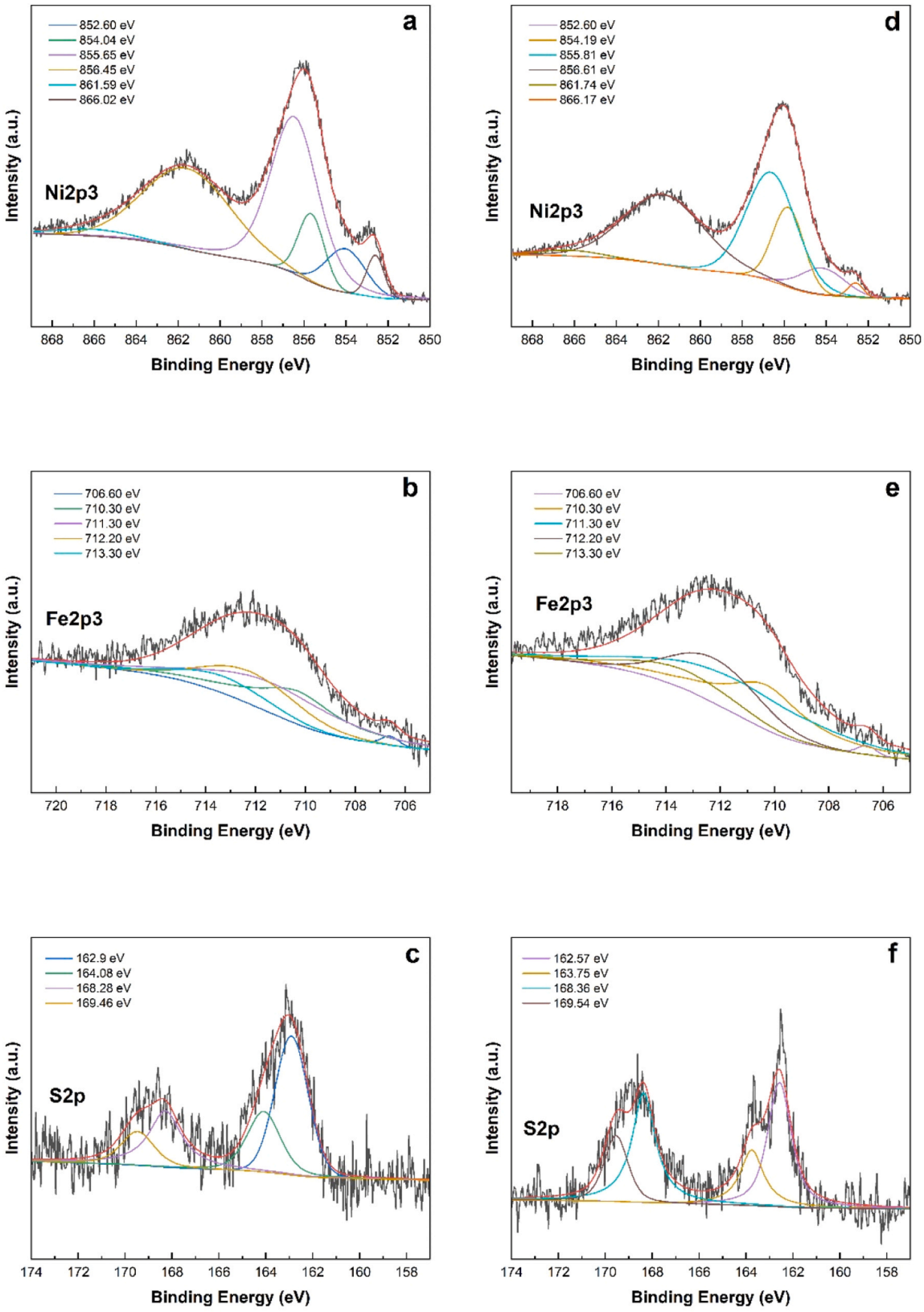

Fig. 4. High-resolution XPS spectra of NiFeS nanowires before and after thermal treatment. (a–c) NiFeS NW: a) Ni 2p, b) Fe 2p, and c) S 2p . (d–f) NiFeS HT150: d) Ni 2p, e) Fe 2p, and f) S 2p . The experimental data (grey) fitted curves (red), and individual fitted components are shown.

spectrum (Fig. 4f) shows a decrease in the relative intensity of the sulphide-related peaks and a concomitant increase in the oxidized sulphur components, suggesting further surface oxidation and partial depletion of sulphide species induced by heating. Overall, these results indicate that the NiFeS surface is already significantly oxidized in the as-prepared state, and that thermal treatment mainly promotes sulphur oxidation without substantially altering the chemical states of Ni and Fe.

The NiFeS electrode was tested in 30 wt% KOH via cyclic voltammetry (CV) at varying scan rates to quantify specific capacitance through the double-layer method. [46]. The quantification of specific capacitance, which is proportional to electrochemically active surface area (ECSA), enabled benchmarking of NiFeS NWs against planar Ni foil. Also, the annealed sample at 150°C was tested. The CV was performed in the non-Faradaic window (0.645–0.795 V vs. RHE, 10–100 mV s^{-1} scan rates) and the Δj at 0.75 V RHE vs was calculated. A linear fit of Δj vs. scan rate gave slopes ~10 times steeper for NWs, evidencing their large active surface area from nanostructured morphology (Fig. 5) [48]. The measured values for as prepared and annealed samples are very similar, indicating that the thermal treatment does not significantly alter the accessible surface area, while preserving the high surface area characteristic of the nanowire architecture.

To estimate the electrocatalytic electrodes behaviour, Quasi Steady State Polarization (QSSP) tests were performed for OER (0.1667 mV s^{-1} scan rate; 1.1–1.8 V vs. RHE, near thermodynamic potential). Ternary NiFeS NW electrodes were compared with NiFe binary alloy electrodes to gauge the impacts of S incorporation.

The results of QSSPs for OER are shown in Fig. 6. Electrode performance was evaluated through the overpotentials at 10 and 100 mA cm^{-2} (η_{10} and η_{100}) [49]. The values were reported in Table 2.

Optimal OER activity emerged from NiFeS NWs synthesized with 15 gL^{-1} $Na_2S_2O_3$ (17 at% S). However, prolonged exposure to KOH caused sulphur leaching and performance degradation.

To avoid sulphur leaching, the samples were thermally treated at different temperatures, as shown in Fig. S2. Among the investigated conditions, post-synthesis annealing at 150 °C (denoted NiFeS HT_{150}) provided the best balance between activity and stability, yielding nearly identical catalytic activity to the as-prepared sample while greatly improving durability. Even after 125 h of operation at 50 mA cm^{-2}, the annealed electrode outperformed the binary NiFe reference. In contrast, higher-temperature annealing led to increased alloy crystallinity and consequently poorer electrochemical performance.

The linear portions of the QSSP curves were fitted to the Tafel equation $\eta = a + b \log i$, where a is related to the exchange current density and b is the Tafel slope.

NiFeS NWs from 15 g L^{-1} $Na_2S_2O_3$ displayed the lowest onset potential (1.569 V) and superior kinetics (Tafel slope (~30 mV dec^{-1}), indicating facile OER via reversible NiFeS-to-NiFeS oxysulfide transformation [50]. The addition of S promotes OH^- adsorption, hastening the rate-determining step (M–O → M–OOH) [51].

NiFeS NW performance aligns competitively with state-of-the-art benchmarks (Table S2), matching or surpassing prior NiFeS reports. Notably, their 30 mV Tafel slope is lower than typical NiFeS alloy values, while η_{10} (at 10 mA/cm^2) value confirms superiority [52]. Once again, the NiFeS NW electrodes exhibit performances that are comparable to or exceed those reported by other authors. Superior OER on NiFeS NW electrodes stems from their elevated electrochemically active surface area (ECSA) and amorphous structure, which offers a major quantity of active catalytic sites for the OER.

The turnover frequency (TOF) was determined using

$$TOF = \frac{iA}{xnF}$$

where i is the current density at a given overpotential, A is the electrochemically active surface area (ECSA) estimated from the double-layer capacitance measurement, F is the Faraday constant (96,485 C mol^{-1}), x is the number of transferred electrons for each molecule of gas produced (4 for OER), and n corresponds to the NiFeS moles, assuming that all NiFeS units are catalytically accessible [53]. The ECSA was estimated from the double-layer capacitance C_{DL} according to:

$$ECSA = \frac{C_{DL}}{C_S}$$

where C_S is the specific capacitance of a smooth surface. A value of 40 μFcm^{-2} was adopted, in accordance with the common practice reported for Ni-based, NiFe-based, and sulphide-derived electrocatalysts operating in alkaline media. The same C_S value was applied to both the as-prepared NiFeS and thermally treated NiFeS HT_{150} electrodes, since the thermal treatment did not significantly alter the nanowire morphology, elemental composition, amorphous character, or double-layer capacitance of the electrodes. Thus, the same interfacial specific capacitance was assumed for both samples [54,55].

It should be noted that this represents a formal TOF estimate based on the total catalyst amount, rather than a true site-specific TOF. In Fig. 7, the TOF related to a NiFe NW electrode is also reported to make a comparison between the two alloys. Considering that the two electrodes have an almost identical morphology, the differences between the two curves can be attributed to the different performance of the two alloys. At identical potentials, the NiFeS NWs exhibited higher TOF values than the NiFe NWs, confirming the beneficial role of sulphur in promoting OH^- oxidation to O_2.

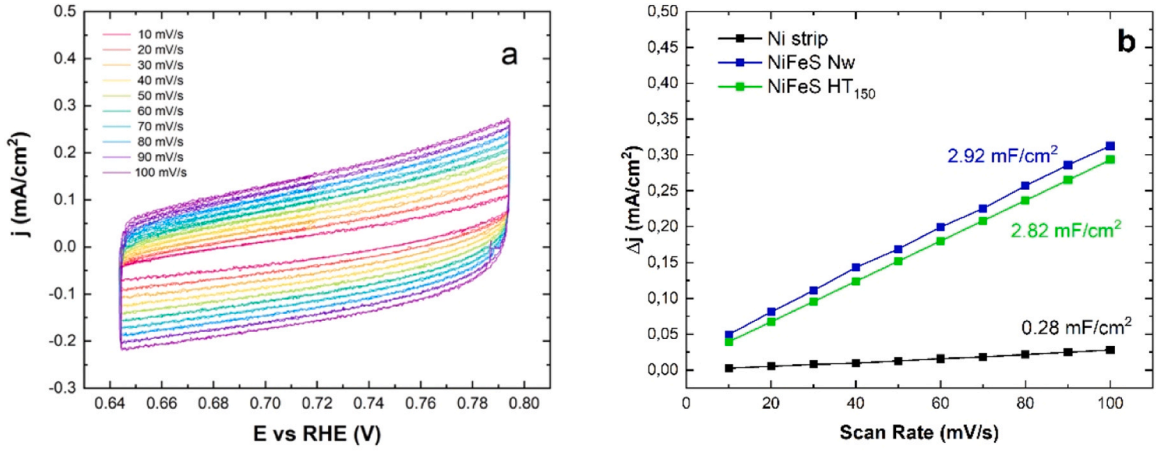

Fig. 5. a) CVs of NiFeS NWs at different scan rates; b) Specific capacitance determined by the double-layer capacitance method: black, Ni foil; blue, NiFeS NWs; green, NiFeS HT_{150}.

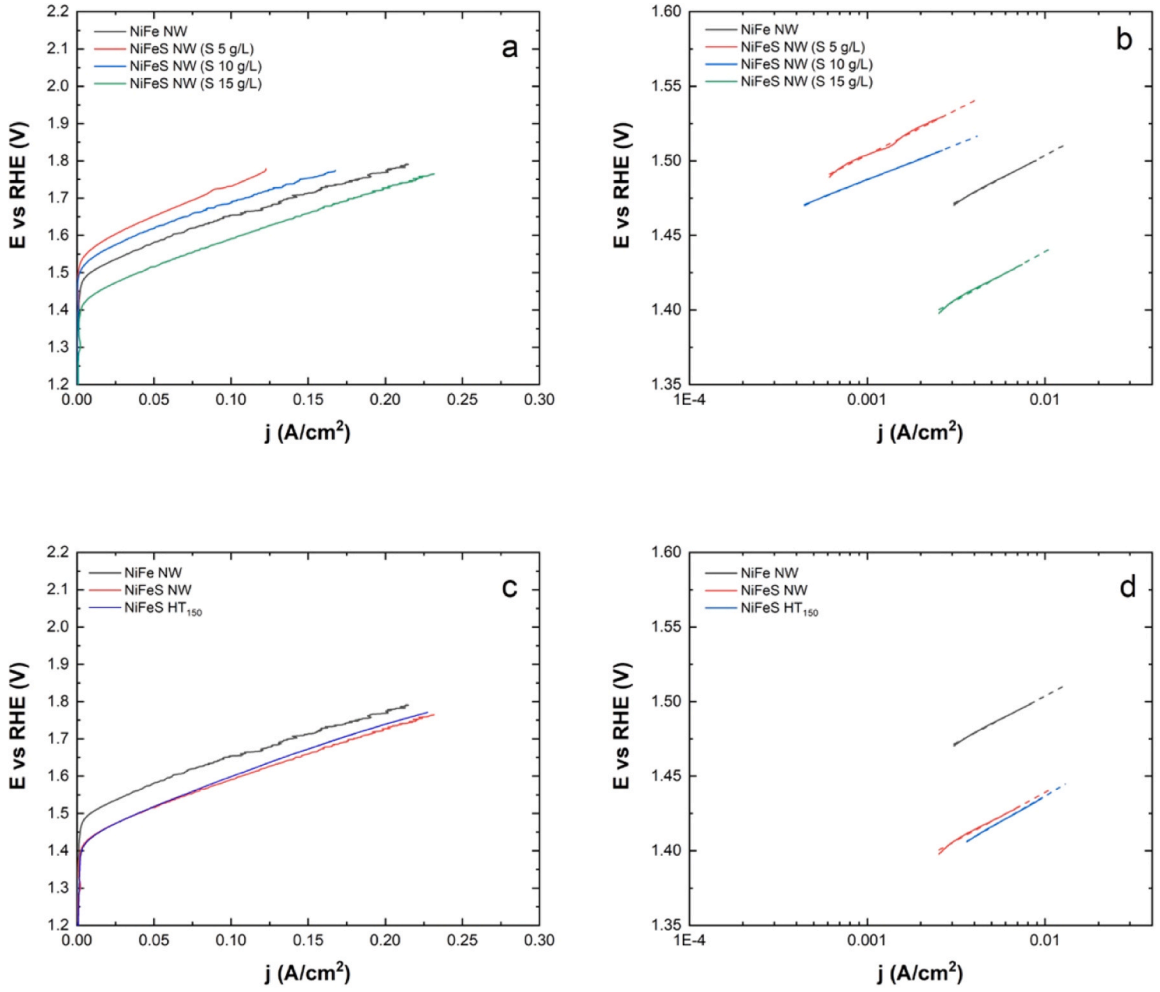

Fig. 6. Quasi-steady-state polarization (QSSP) curves for OER at 0.1667 mV s^{-1} : a) NiFeS NWs at different compositions compared to NiFe NWs; b) linear region of a); c) best-performing NiFeS NWs after 150 °C treatment vs. NiFe NWs; d) linear region of c).

Table 2
Overpotentials η_{10} and η_{100} for OER on NiFe and NiFeS NW electrodes.

	η_{10}	η_{100}
NiFe NW	273 mV	424 mV
NiFeS NW (5 g/L)	334 mV	502 mV
NiFeS NW (10 g/L)	309 mV	458 mV
NiFeS NW (15 g/L)	208 mV	360 mV
NiFeS NW HT_{150}	206 mV	368 mV
NiFeS NW HT_{150} after 125 h of testing in KOH	230 mV	409 mV

The behaviour of the NiFeS NW electrodes at high current densities was studied using galvanostatic step polarization. These tests were carried out using a multi-step current protocol in which the current density was progressively increased, with each step lasting 300 s, ranging from 10 to 500 mA cm^{-2} (10, 20, 50, 100, 200, 500). In Fig. 8, data points reflect mean potentials recorded across individual chronopotentiometric steps. The results obtained with step galvanostatic polarization are very similar to the curves obtained with QSSP tests, demonstrating that the obtained results are robust.

The stability over time was evaluated by performing a mid-term stability test at constant current density, conducted for 6 h at 50 mA cm^{-2} for the OER. Fig. 9a displays time-averaged potentials (over 1800 s per point), evidencing robust stability across the 6 h test for both NiFeS and NiFeS HT_{150} electrodes, with the potential remaining almost constant at the value of 1.549 V vs RHE throughout the 6 h. A further investigation was performed to verify long-term stability (125 h), Fig. 9b (over 5 h per point). For the NiFeS NW electrode, the long-term test reveals unstable performance, with the potential drifting from 1.570 V to 1.751 V vs RHE, corresponding to a total increase of 181 mV.

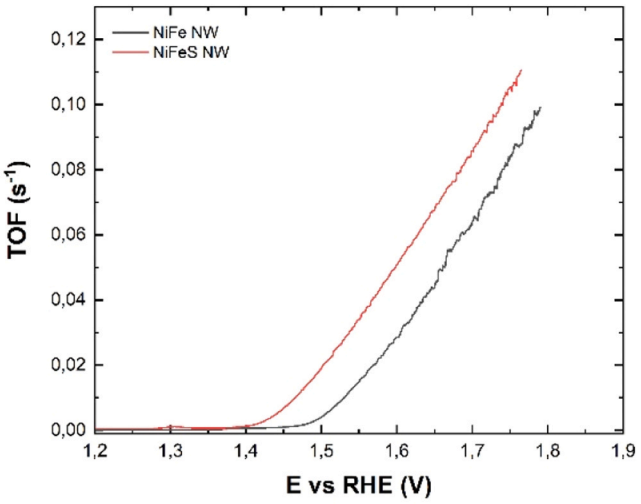

Fig. 7. Turnover frequency (TOF) values for OER on NiFeS NWs and planar Ni foil in 30 wt% KOH.

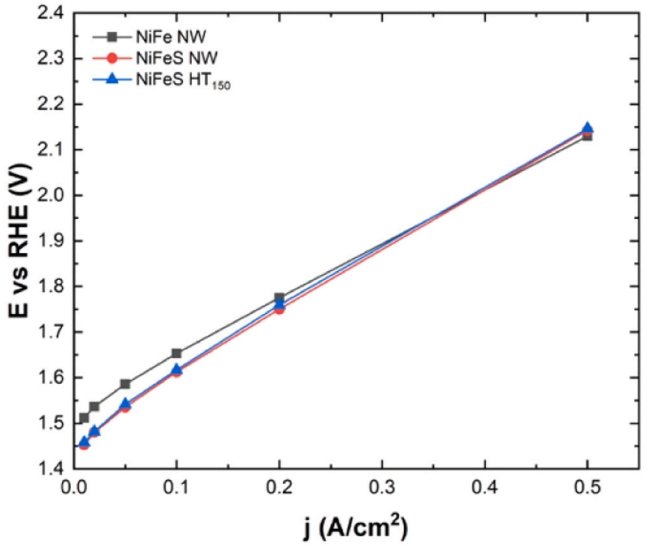

Fig. 8. Galvanostatic-step polarization for OER in 30% wt KOH.

This behaviour is ascribed to sulphur leaching in KOH, which degrades the activity of the NiFeS alloy, since it operates as a binary Ni-rich alloy with a higher nickel content that, as demonstrated in our previous work, exhibits the worst performance. In contrast, the NiFeS HT_{150} electrode shows markedly improved stability, with the potential changing only from 1.556 V to 1.589 V vs RHE over 125 h, for a total loss of 33 mV. This enhanced stability is attributed to the heat treatment, which, thanks to its low temperature, preserves the amorphous structure of the catalyst while immobilizing sulphur within the alloy matrix (Table 3).

Such stabilization suppresses sulphur leaching and, in turn, improves the electrochemical performance of the electrode and long-term durability under harsh alkaline conditions.

Electrodes tested for 125 h were characterized by SEM, EDS, and XRD to assess their stability. Fig. 9 shows that the nanowire array morphology was largely preserved, with only minor mechanical fractures in some areas (Fig. 10b).

EDS analysis, however, revealed changes in alloy composition (Table 4). Sulphur content decreased markedly for untreated NiFeS NWs (from 17.1 to 3.0 at%), while annealed NiFeS HT_{150} retained a substantial fraction (12.9 at%). As reported above, these results were also confirmed by ICP-OES (Table S1). The reduction of the sulphur content in the NiFeS alloy during operation in KOH is the synergistic result of processes of chemical leaching and electrochemical oxidation [56]. First, the sulphur initially present in the alloy in the form of metal sulphides (NiS, FeS or mixed phases) is subject to chemical leaching in an alkaline environment. Under these conditions, metal sulphides react with OH^- ions to form soluble species such as HS^- and S^{2-}.

Secondly, under anodic operating conditions (e.g., during the OER), sulphur can be further electrochemically oxidized to more oxidizing soluble compounds (such as $S_2O_3^{2-}$), which do not remain bound to the solid structure and are dispersed in the solution. This process accelerates the loss of sulphur from the active surface of the catalyst [57].

In contrast, the post-heat-treatment samples exhibit greater stability, retaining a substantial sulphur fraction even after 125 h in 30 wt% KOH. This enhanced stability arises from the formation of more stable phases, such as FeS_2, during heat treatment; these phases feature stronger M–S bonds that resist chemical leaching and promote better sulphur integration into the metal matrix. The improved stability also stems from reduced surface defects (which serve as preferential sites for hydroxide ions reaction) and the lower solubility of thermal-treated sulphur phases compared to untreated ones, which curtails conversion to soluble species [58]. XRD patterns after stability testing (Fig. S3) were nearly identical to the pristine ones, confirming structural integrity. Two peaks with very low intensity at about 11.2° and 22.8°. These peaks are characteristic of the layered structure of a NiFe oxy-hydroxide of the LDH (layered double hydroxide) type, exhibiting low crystallinity (broad and weak diffraction bands) [59]. Their low intensity and broadening are indicative of a partially amorphous or nanocrystalline nature. The formation of NiFe oxy-hydroxide is also reported in previous studies [60,61].

Raman spectroscopy was performed on the as-deposited (RT), thermally treated (HT_{150}), and post-OER samples to further investigate the structural nature of the NiFeS alloy. As shown in Fig. 11, all spectra exhibit broad bands rather than sharp, well-defined peaks, indicating the absence of long-range crystalline order and supporting the predominantly amorphous nature of the material. This amorphous character is preserved after thermal treatment at 150 °C, since no sharp Raman features emerge in the HT_{150} sample, suggesting only limited

Table 3
Tafel parameters for OER in 30 wt% KOH.

	a (V)	*b* (V/dec)	R^2 (%)
NiFe NW	1.629	0.027	99.90
NiFeS NW (5 g/L)	1.685	0.026	99.60
NiFeS NW (10 g/L)	1.628	0.022	99.96
NiFeS NW (15 g/L)	1.569	0.026	99.57
NiFeS NW HT_{150}	1.575	0.030	99.94
NiFeS NW HT_{150} after 125 h of testing in KOH	1.576	0.021	99.97

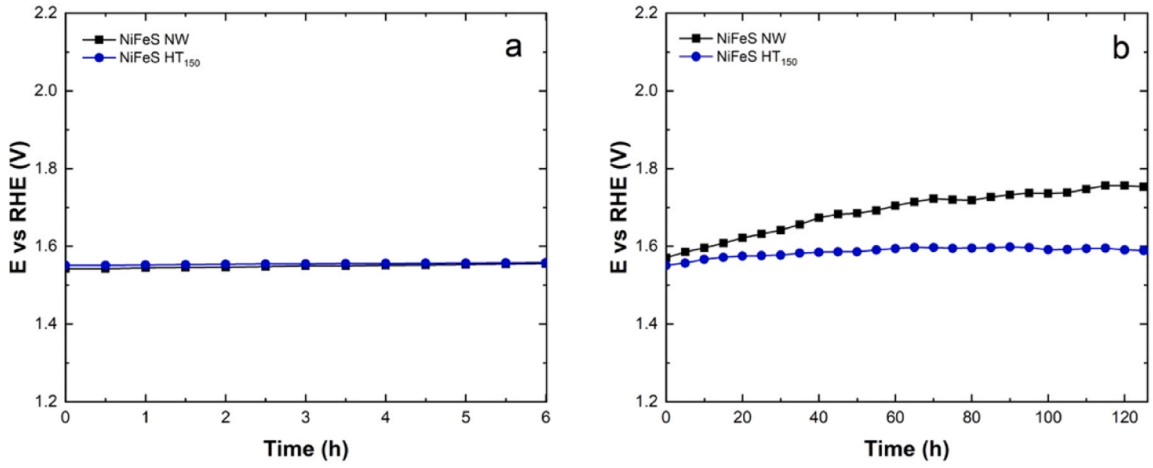

Fig. 9. a) Mid-term stability test for 6 h for OER at 50 mA cm^{-2} and b) Long-term stability test for 125 h for OER at 50 mA cm^{-2} in 30% wt KOH.

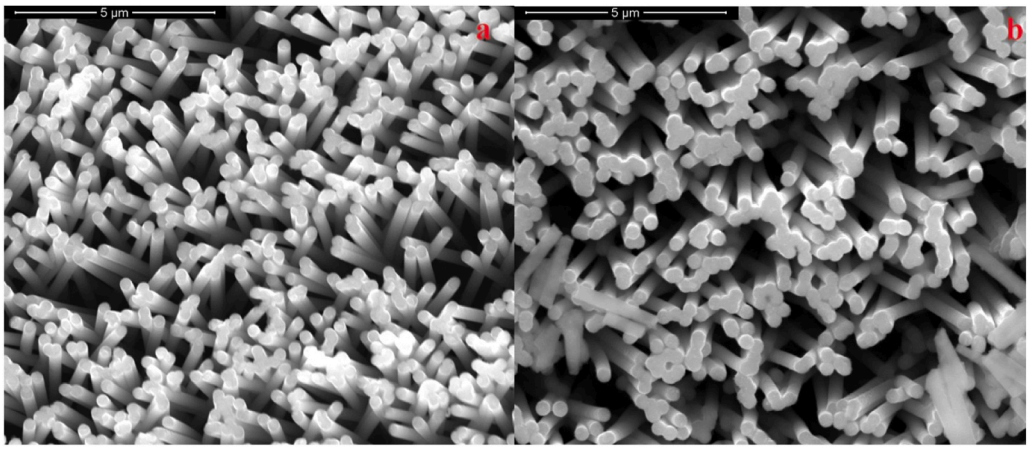

Fig. 10. SEM images after 125 h OER in 30 wt% KOH: (a) NiFeS NWs; (b) NiFeS HT_{150} NWs.

Table 4
Composition of NiFeS alloy by EDS analysis after OER (SD 2%).

Element (at%)	NiFeS NW before OER	NiFeS NW after OER	NiFeS NW HT_{150} before OER	NiFeS NW HT_{150} after OER
Ni	76.1	87.29	77.09	76.62
Fe	6.8	9.70	6.33	10.53
S	17.1	3.01	16.58	12.85
Total	100	100	100	100

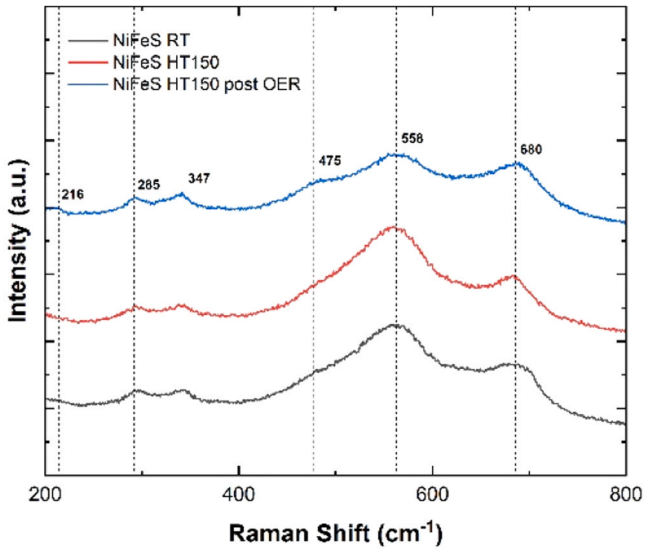

Fig. 11. Raman spectra of NiFeS nanowire electrodes in the as-deposited state (black), after thermal treatment at 150 °C (red), and after OER test (blue).

structural rearrangement without crystallization. In the RT sample, bands around ~285 cm^{-1} may be associated with Fe–S vibrations [62], while features at ~347 and ~558 cm^{-1} can be assigned to Ni–S vibrational modes, consistent with NiS-like local coordination [63,64]. A broader band at ~680 cm^{-1} may be related to Fe–O vibrations, suggesting the presence of partial surface oxidation under ambient conditions [65]. These features are retained after thermal treatment, indicating that the samples remain largely unchanged.

After the OER test, additional spectral modifications are observed. A weak feature at ~211 cm^{-1} can be attributed to Fe–S vibrations [62], while a shoulder near ~475 cm^{-1} may be associated with Ni–O vibrations, suggesting the formation of nickel oxide or oxyhydroxide species during electrochemical operation [66]. Moreover, the band at ~680 cm^{-1} , becomes more intense, consistent with further oxidation of iron species under anodic conditions. These changes suggest the formation of surface oxide/oxyhydroxide phases during OER, which are commonly considered active species for oxygen evolution.

The performance of NiFeS alloy electrodes was also evaluated under conditions simulating coupling with a photovoltaic-powered electrolyzer system (Fig. 12). The test reproduced a realistic day–night cycle, consisting of 8 h of simulated light (operation) followed by 16 h of dark (shutdown), repeated over 7 days.

Under these conditions, the NiFeS NW electrodes exhibited a marked performance decline starting from the third day, with progressive increases in operating potential during each 8 h activation window, indicating limited long-term stability. Unlike untreated NiFeS, HT_{150}-treated variants sustained steady potential over the full test, underscoring how 150 °C annealing markedly bolsters durability for fluctuating loads in solar-driven electrolyzers.

To evaluate the practical applicability of the NiFeS NW electrodes, they were tested as bifunctional electrodes in a lab-scale alkaline electrolyzer under realistic operating conditions (Fig. S4–6). NiFeS NWs were compared with NiFe-based electrodes, and the setup consisted of an alkaline electrolysis cell equipped with a recirculation pump using 30 wt% KOH. The linear sweep voltammetry (LSV) curves shown in

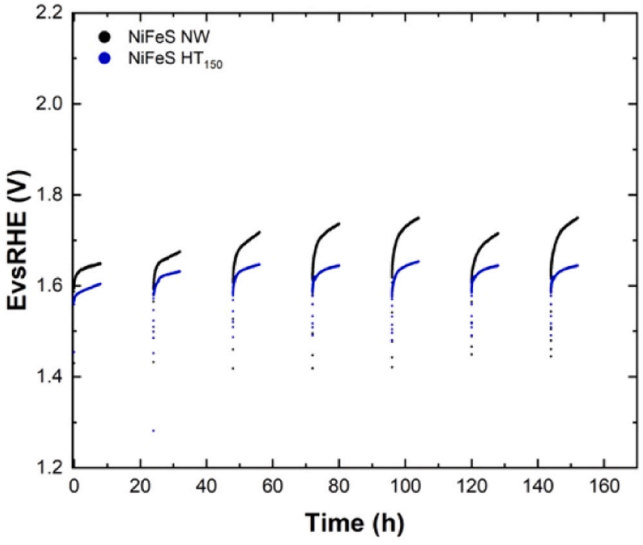

Fig. 12. Simulated electrolyzer/photovoltaic coupling test for OER in 30 wt% KOH (8 h light/16 h dark cycles over 7 days).

Fig. S6 indicate that a current density of 10 mA cm^{-2} is reached at only 1.65 V for the electrolyzer with NiFeS NW electrolyzer, which is lower than that required for the NiFe counterpart. This result confirms the improved performance of the NiFeS nanostructured electrodes in this configuration.

Continuous operation was evaluated at 100 mA cm^{-2} and 25 °C for 125 h, Fig. 13a, with each data point representing the average potential recorded over 3600 s. Under these conditions, a stable cell potential of about 1.94 V was maintained, and the NiFeS NW electrodes display very stable performance, with an overall increase of only 30 mV over the entire test. After long-term operation, multistep chronopotentiometry measurements (Fig. 13b) showed only a slight deviation of less than 30 mV at 0.5 A cm^{-2}, confirming the excellent stability of the electrodes.

Post-test SEM analysis (Fig. S7) showed that the nanowire morphology was preserved across the electrode surface, although the nanowire surfaces appeared more wrinkled and were covered with needle-like features, likely corresponding to a thin NiFe layered double hydroxide layer, in agreement with previous reports [60,61]. These observations are consistent with the XRD results in Fig. S3. In addition, post−125h EDS mapping of individual NWs (Fig. S8) confirmed the homogeneous distribution of Ni, Fe, and S along the full nanowire length, and the EDS data in Table S3 further support the retention of all three elements after prolonged operation. Notably, the thermally treated anode still retained a substantial sulphur fraction after 125 h in 30 wt% KOH. In the XPS spectra of Fig. S9, according to the results reported in [67], some spectral changes are observed, suggesting partial surface oxidation during electrochemical operation, while the overall amorphous character of the material is preserved.

During electrolyzer operation, gas evolution measurements were also carried out to determine the Faradaic efficiency (Fig. S10). The measured oxygen production rates at current densities of 100 and 200 mA cm^{-2}, yielding values of 1.49 and 3.02 mL min^{-1} , respectively, in excellent agreement with the theoretical values calculated from the applied current, corresponding to an efficiency of approximately 98–99%. These results indicate that the measured current is almost entirely associated with water oxidation, with negligible contribution from parasitic reactions. Overall, the full-cell tests demonstrate that the improved activity and stability of the NiFeS NW electrodes are maintained under practical alkaline electrolyzer conditions, supporting their relevance for real-device applications.

Table S4 shows the estimated costs for manufacturing NiFeS-based electrodes. Based on laboratory cost estimates, a value of €0.27 cm^{-2} was calculated for NiFe NW-based electrodes. Comparing this value with those reported for foam and SS 316 substrates highlights the cost advantages of nanowire electrodes fabricated via a template-assisted deposition.

4. Conclusions

This work demonstrates a template-assisted route to composition-optimized NiFeS nanowires, combined with low-temperature thermal stabilization, to obtain durable electrodes suitable for practical alkaline water electrolysis. The NiFeS composition with 17% sulphur and 7% iron displayed the best OER performance among the tested samples, confirming the strong capabilities of NiFeS due to its high density of active sites and favourable electronic structure. Despite high initial activity, long-term galvanostatic tests at 50 mA cm^{-2} (6 and 125 h) revealed stability losses in untreated samples during OER, mainly from sulphur leaching out of the amorphous alloy matrix. To address this, a post-synthesis thermal treatment was applied. The 150 °C treated electrodes exhibited marked improvements in durability, preserving structural integrity and sulphur content during extended operation by stabilizing sulphur species within the alloy and maintaining the nanostructured morphology. Overall, these nanostructured NiFeS electrodes emerge as highly active OER materials, while the template-assisted pulsed electrodeposition approach offers a controllable and reproducible route to fabricate uniform nanowire architectures. The thermal treatment represents an effective strategy to enhance durability, and future work should focus on simplifying the process, reducing template-related costs, and scaling up the deposition area to further assess its practical feasibility for alkaline water electrolyzers.

CRediT authorship contribution statement

Nadia Moukri: Methodology, Investigation. **Oliveri Roberto:** Writing – original draft, Investigation, Data curation, Conceptualization. **Bernardo Patella:** Methodology, Formal analysis, Data curation. **Salvatore Geraci:** Writing – original draft, Methodology, Investigation. **Myeongsub Kim:** Writing – review & editing, Supervision, Conceptualization. **Rosalinda Inguanta:** Writing – review & editing, Supervision, Funding acquisition, Formal analysis, Data curation, Conceptualization. **Priyadharshini Matheswaran:** Writing – original draft, Methodology, Investigation, Data curation. **Philippe Mandin:** Writing – review & editing, Supervision, Formal analysis, Conceptualization. **Filippo Pellitteri:** Methodology, Investigation. **Rosario Miceli:** Supervision, Project administration, Funding acquisition, Conceptualization.

Declaration of Competing Interest

The authors declare that they have no known competing financial

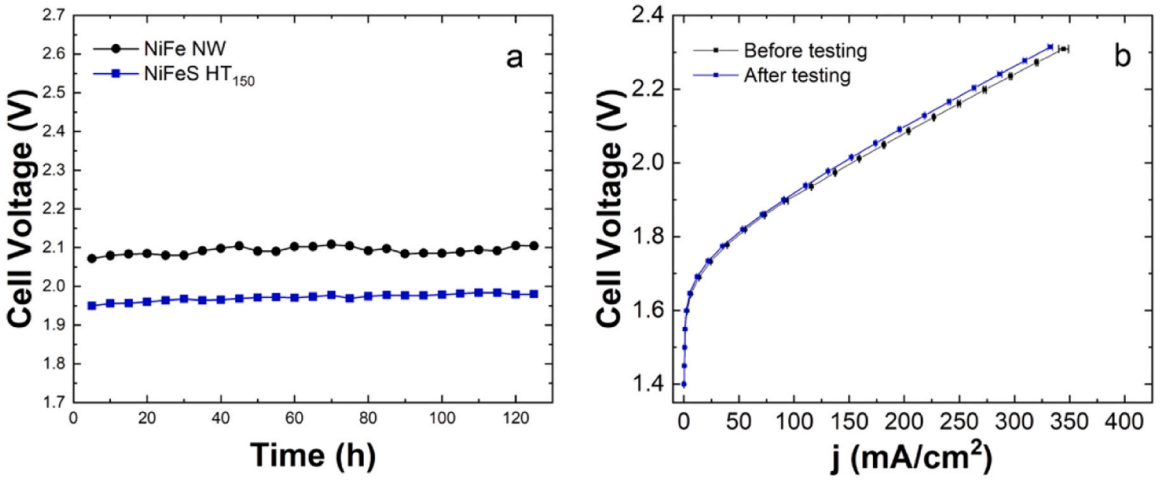

Fig. 13. a) The stability curve of the AWE at a current density of 100 mA cm^{-2} for NiFe and NiFeS NWs.; b) Potentiostatic test before and after 125 h.

interests or personal relationships that could have appeared to influence the work reported in this paper.

Acknowledgements

This work was supported by the project PUSH2Green (RSH2A_000019, Italian Ministry of Environment and Energy Security – MASE), within the National Recovery and Resilience Plan (PNRR), Mission 2 “Green Revolution and Ecological Transition”, Component 2 “Renewable Energy, Hydrogen, Network and Sustainable Mobility”, Investment 3.5 “Hydrogen Research and Development”, European Union – NextGenerationEU.

Appendix A. Supporting information

Supplementary data associated with this article can be found in the online version at doi:10.1016/j.jallcom.2026.189252.

References

[1] R. Aguado Molina, J.J. Cartelle Barros, M.D.P. De La Cruz López, M. Lara Coira, A. Del Caño Gochi, A comparative sustainability assessment of several grid energy storage technologies, Appl. Energy 396 (2025) 126248, https://doi.org/10.1016/j.apenergy.2025.126248.
[2] C. Karakosta, J. Papathanasiou, Decarbonizing the construction sector: strategies and pathways for greenhouse gas emissions reduction, Energies 18 (2025) 1285, https://doi.org/10.3390/en18051285.
[3] A.A. Firoozi, A.A. Firoozi, M.R. Maghami, Harnessing photovoltaic innovation: Advancements, challenges, and strategic pathways for sustainable global development, Energy Convers. Manag. X 27 (2025) 101058, https://doi.org/10.1016/j.ecmx.2025.101058.
[4] C. Anand, B. Chandraja, P. Nithiya, M. Akshaya, P. Tamizhdurai, G. Shoba, A. Subramani, R. Kumaran, K.K. Yadav, A. Gacem, J.K. Bhutto, M.A. Alreshidi, M. W. Alam, Green hydrogen for a sustainable future: A review of production methods, innovations, and applications, Int. J. Hydrog. Energy 111 (2025) 319–341, https://doi.org/10.1016/j.ijhydene.2025.02.257.
[5] N. Subedi, M.M. Hossain Bhuiyan, M.A. Islam, B.C. Alfredo, Z. Siddique, Hydrogen as an energy carrier: Production pathways, thermochemical constraints, and electrolysis-based green hydrogen prospects, Int. J. Hydrog. Energy 220 (2026) 154100, https://doi.org/10.1016/j.ijhydene.2026.154100.
[6] I.M.S. Anekwe, S.I. Mustapha, S.O. Akpasi, E.K. Tetteh, A.S. Joel, Y.M. Isa, The hydrogen challenge: addressing storage, safety, and environmental concerns in hydrogen economy, Int. J. Hydrog. Energy 167 (2025) 150952, https://doi.org/10.1016/j.ijhydene.2025.150952.
[7] F.A. Ahmed Ali, F. Fadhillah, A.M. Alghamdi, T.V. Kumar, S. Padmanabhan, P. Saravanan, S. Ganesan, A.I. Alromaeh, A.A. Assadi, W.A.M. Al-Garadi, G. Shoba, P. Tamizhdurai, Clean hydrogen from water: emerging technologies for a sustainable energy future, RSC Adv. 16 (2026) 29073–29120, https://doi.org/10.1039/D6RA03255A.
[8] X. Ma, X. Zhang, Y. Ge, Y. Yang, Y. Xu, B. Zhou, Simulation Modeling and Comparative Analysis of Multi-Type Electrolytic Hydrogen Production Methods, in: Q. Yang, Z. Bie, X. Yang (Eds.), Proc. 19th Annu. Conf. China Electrotech. Soc., Springer Nature Singapore, Singapore, 2025, pp. 453–468, https://doi.org/10.1007/978-981-96-1391-5_45.
[9] E.N. Aminaho, N.S. Aminaho, F. Aminaho, Techno-economic assessments of electrolyzers for hydrogen production, Appl. Energy 399 (2025) 126515, https://doi.org/10.1016/j.apenergy.2025.126515.
[10] B. Łosiewicz, Advanced Electrode Materials for Water Electrolysis: Design Principles, Performance Trade-Offs, and Technology Pathways Across ALK, PEM, SOEC, and AEM Systems, Materials 19 (2026) 2259, https://doi.org/10.3390/ma19112259.
[11] R. Wu, R. Gao, Z. Li, J. Wang, H. Wang, Y. Wu, S. Jiang, X. Zhang, X. Wang, X. Liu, Z. Lu, Nanoporous high-entropy Mn-Fe-Co-Ni amorphous oxide: Boosting oxygen evolution efficiency through electron spin-polarization, J. Mater. Sci. Technol. 238 (2025) 266–275, https://doi.org/10.1016/j.jmst.2025.03.050.
[12] M. Ismael, Recent developments of hydrogen and oxygen evolution electrocatalysts in proton electrolyte membrane water electrolyzers (PEMWE), Results Eng. 29 (2026) 109564, https://doi.org/10.1016/j.rineng.2026.109564.
[13] W. Wang, C. Chen, Z. Liu, Q. Zhu, Y. Xu, Z. Lu, B. Zhang, Z. Yu, G. Xu, From laboratory to industrial scale: nickel-based catalysts for hydrogen evolution under highcurrent–density alkaline electrolysis, Rare Met. 44 (2025) 9507–9542, https://doi.org/10.1007/s12598-025-03624-0.
[14] X. Zhang, J. Wang, K. Zong, Z. Chen, X. Yang, L. Yang, X. Wang, Z. Chen, Recent advances in non-noble metal-based electrocatalysts for hybrid water electrolysis systems, Carbon Energy 7 (2025) e679, https://doi.org/10.1002/cey2.679.
[15] S. Elsharkawy, P. Żabiński, Effect of Fe/Ni ratio on electrodeposition of Ni-Fe alloys and their bifunctional catalytic performance in hydrogen and oxygen evolution reactions, J. Power Sources 660 (2025) 238516, https://doi.org/10.1016/j.jpowsour.2025.238516.
[16] J. Corbin, C. Lyu, D. Trudgeon, M. Jones, A. Loh, A. Graf, Z. Zhang, J. Cao, I. Nawrocka, X. Li, Systematic study of electrochemical performance of nickel iron hydroxide ($NiFe(OH)_2$) electrocatalyst at high current densities in alkaline seawater solutions, RSC Sustain. 4 (2026) 493–510, https://doi.org/10.1039/D5SU00650C.
[17] B. Feng, Y. Hao, J. Chen, H. Wang, C. Zhong, Y. Yang, Y. Yao, Nanostructured NiFe (oxy)hydroxide fabricated on nickel foams by laser-induced water plasma for enhanced alkaline oxygen evolution reaction, Appl. Surf. Sci. 622 (2023) 156934, https://doi.org/10.1016/j.apsusc.2023.156934.
[18] X. Wang, J. Wang, X. Sun, S. Wei, L. Cui, W. Yang, J. Liu, Hierarchical coral-like NiMoS nanohybrids as highly efficient bifunctional electrocatalysts for overall urea electrolysis, Nano Res. 11 (2018) 988–996, https://doi.org/10.1007/s12274-017-1711-3.
[19] J.N.Y. Bamba, M.F. Divinagracia-Luzadas, D. Yoon, J. Choi, J.D. Ocon, J. Lee, Recent progress in NiFe-based catalysts for the high current density oxygen evolution reaction, Chem. Commun. 62 (2026) 4889–4901, https://doi.org/10.1039/D5CC06703K.
[20] M. Durai, M. Durai, E. Erusappan, S. Gopi, K. Yun, Advances in MOF-derived porous carbons, oxides, and hybrids for water splitting and beyond, J. Eur. Ceram. Soc. 46 (2026) 118156, https://doi.org/10.1016/j.jeurceramsoc.2026.118156.
[21] W. Xu, J.-P. Zhang, X.-Q. Tang, X. Yang, Y.-W. Han, M.-J. Lan, X. Tang, Y. Shen, Highly efficient sulfur-doped Ni3Fe electrocatalysts for overall water splitting: Rapid synthesis, mechanism and driven by sustainable energy, J. Colloid Interface Sci. 653 (2024) 1423–1431, https://doi.org/10.1016/j.jcis.2023.10.003.
[22] J. Jiang, Y. Xu, Z. Wang, H. Zhang, Q. Xu, Y. Li, High-entropy nitrides from dual entropic and enthalpic forces for high-efficiency oxygen evolution reaction, Energy Mater. 5 (2025), https://doi.org/10.20517/energymater.2024.130.
[23] C. Miao, X. Zheng, J. Sun, H. Wang, J. Qiao, N. Han, S. Wang, W. Gao, X. Liu, Z. Yang, Facile Electrodeposition of Amorphous Nickel/Nickel Sulfide Composite Films for High-Efficiency Hydrogen Evolution Reaction, ACS Appl. Energy Mater. 4 (2021) 927–933, https://doi.org/10.1021/acsaem.0c02863.
[24] S. Liu, Y. Wang, J. Gao, W. Jin, W. Xiao, L. Xin, Z. Xiao, G. Xu, C. Dai, H. Zhang, Z. Wu, L. Wang, Anionic phosphorous and sulfur regulate self-supported Ni-Fe-based electrocatalyst for water-splitting under large current density, Fuel 367 (2024) 131445, https://doi.org/10.1016/j.fuel.2024.131445.
[25] Y. Wei, J. Cheng, Q. Yang, S. Wang, X. Chen, B. Li, B. Zou, Synthesis of hierarchically structured nickel–iron sulfide on nickel foam as a catalyst for efficient oxygen evolution reaction, Int. J. Electrochem. Sci. 20 (2025) 101051, https://doi.org/10.1016/j.ijoes.2025.101051.
[26] S. Gao, Z. Wang, P. Nie, J. Jian, H. Wang, F. Yao, L. Chang, Construction of nickel iron sulfide at ambient temperature on Fe foam for high-current overall water splitting, Catal. Sci. Technol. 14 (2024) 3559–3566, https://doi.org/10.1039/D4CY00328D.
[27] E. López-Fernández, J. Gil-Rostra, J.P. Espinós, A.R. González-Elipe, A. De Lucas Consuegra, F. Yubero, Chemistry and Electrocatalytic Activity of Nanostructured Nickel Electrodes for Water Electrolysis, ACS Catal. 10 (2020) 6159–6170, https://doi.org/10.1021/acscatal.0c00856.
[28] S. Carbone, F. Proietto, F. Bonafede, R.L. Oliveri, B. Patella, F. Ganci, G. Aiello, P. Mandin, M. Kim, M. Scopelliti, R. Inguanta, Behavior of a forest of NiFe nanowires in KOH and NaCl solution for water electrolysis, Electrochim. Acta 467 (2023) 143120, https://doi.org/10.1016/j.electacta.2023.143120.
[29] K. Singh, K. Selvaraj, Tensile nanostructured hierarchically porous non-precious transition metal-based electrocatalyst for durable anion exchange membrane-based water electrolysis, J. Colloid Interface Sci. 664 (2024) 389–399, https://doi.org/10.1016/j.jcis.2024.02.170.
[30] E.P.C. Higgins, A.A. Papaderakis, C. Byrne, R. Cai, A. Elgendy, S.J. Haigh, A. S. Walton, D.J. Lewis, R.A.W. Dryfe, High-Performance Nanostructured MoS_2 Electrodes with Spontaneous Ultralow Gold Loading for Hydrogen Evolution, J. Phys. Chem. C. 125 (2021) 20940–20951, https://doi.org/10.1021/acs.jpcc.1c06733.
[31] B. Buccheri, F. Ganci, B. Patella, G. Aiello, P. Mandin, R. Inguanta, Ni-Fe alloy nanostructured electrodes for water splitting in alkaline electrolyser, Electrochim. Acta 388 (2021) 138588, https://doi.org/10.1016/j.electacta.2021.138588.
[32] P. Hao, Y. Xin, J. Tian, L. Li, J. Xie, F. Lei, L. Tong, H. Liu, B. Tang, Novel (Ni, Fe) S2/(Ni, Fe)3S4 solid solution hybrid: an efficient electrocatalyst with robust oxygen-evolving performance, Sci. China Chem. 63 (2020) 1030–1039, https://doi.org/10.1007/s11426-020-9770-5.
[33] T.-R. Lee, L. Chang, C.-H. Chen, Effect of electrolyte temperature on composition and phase structure of nanocrystalline Fe–Ni alloys prepared by direct current electrodeposition, Surf. Coat. Technol. 207 (2012) 523–528, https://doi.org/10.1016/j.surfcoat.2012.07.069.
[34] A. Afshar, A.G. Dolati, M. Ghorbani, Electrochemical characterization of the Ni–Fe alloy electrodeposition from chloride–citrate–glycolic acid solutions, Mater. Chem. Phys. 77 (2003) 352–358, https://doi.org/10.1016/S0254-0584(02)00017-2.
[35] D. Kim, D.-Y. Park, B.Y. Yoo, P.T.A. Sumodjo, N.V. Myung, Magnetic properties of nanocrystalline iron group thin film alloys electrodeposited from sulfate and chloride baths, Electrochim. Acta 48 (2003) 819–830, https://doi.org/10.1016/S0013-4686(02)00773-9.
[36] J.O. Bockris, D. Drazic, A.R. Despic, The electrode kinetics of the deposition and dissolution of iron, Electrochim. Acta 4 (1961) 325–361, https://doi.org/10.1016/0013-4686(61)80026-1.
[37] M. Matlosz, Competitive Adsorption Effects in the Electrodeposition of Iron-Nickel Alloys, J. Electrochem. Soc. 140 (1993) 2272–2279, https://doi.org/10.1149/1.2220807.

[38] Á. Llavona, L. Pérez, M.C. Sánchez, V. De Manuel, Enhancement of anomalous codeposition in the synthesis of Fe–Ni alloys in nanopores, Electrochim. Acta 106 (2013) 392–397, https://doi.org/10.1016/j.electacta.2013.05.116.
[39] O. Dragos, H. Chiriac, N. Lupu, M. Grigoras, I. Tabakovic, Anomalous Codeposition of *fcc* NiFe Nanowires with 5–55% Fe and Their Morphology, Crystal Structure and Magnetic Properties, J. Electrochem. Soc. 163 (2016) D83–D94, https://doi.org/10.1149/2.0771603jes.
[40] A.S. Aliyev, M. El-rouby, Original Article Electrochemical Reduction Studies on the Behavior of Thiosulfate on Multi Walled Carbon Nano Tubes Paste Electrode, (n. d.).
[41] S. Shit, S. Bolar, N.C. Murmu, T. Kuila, Binder-Free Growth of Nickel-Doped Iron Sulfide on Nickel Foam via Electrochemical Deposition for Electrocatalytic Water Splitting, ACS Sustain. Chem. Eng. 7 (2019) 18015–18026, https://doi.org/10.1021/acssuschemeng.9b04882.
[42] M. Hosseini, T. Shahrabi, G.B. Darband, A. Fathollahi, Durable Pulse-Electrodeposited Ni–Fe–S Nanosheets Supported on a Ni–S Three Dimensional Pattern as Robust Bifunctional Electrocatalysts for Hydrogen Evolution and Urea Oxidation Reactions, Langmuir 40 (2024) 2028–2038, https://doi.org/10.1021/acs.langmuir.3c02417.
[43] A.P. Grosvenor, B.A. Kobe, M.C. Biesinger, N.S. McIntyre, Investigation of multiplet splitting of Fe 2p XPS spectra and bonding in iron compounds, Surf. Interface Anal. 36 (2004) 1564–1574, https://doi.org/10.1002/sia.1984.
[44] J.F. Moulder, J. Chastain, Handbook of X-ray photoelectron spectroscopy: a reference book of standard spectra for identification and interpretation of XPS data, Update (eds.), Perkin-Elmer Corporation, Eden Prairie, Minn, 1992.
[45] P. Ganesan, A. Sivanantham, S. Shanmugam, Inexpensive electrochemical synthesis of nickel iron sulphides on nickel foam: super active and ultra-durable electrocatalysts for alkaline electrolyte membrane water electrolysis, J. Mater. Chem. A 4 (2016) 16394–16402, https://doi.org/10.1039/C6TA04499A.
[46] A.J. Bard, L.R. Faulkner, H.S. White. Electrochemical methods: fundamentals and applications, Third edition, Wiley, Hoboken, NJ, USA Chichester, West Sussex, UK, 2022.
[47] M.C. Biesinger, B.P. Payne, A.P. Grosvenor, L.W.M. Lau, A.R. Gerson, R.St. C. Smart, Resolving surface chemical states in XPS analysis of first row transition metals, oxides and hydroxides: Cr, Mn, Fe, Co and Ni, Appl. Surf. Sci. 257 (2011) 2717–2730, https://doi.org/10.1016/j.apsusc.2010.10.051.
[48] K.I. Siwek, S. Eugénio, D.M.F. Santos, M.T. Silva, M.F. Montemor, 3D nickel foams with controlled morphologies for hydrogen evolution reaction in highly alkaline media, Int. J. Hydrog. Energy 44 (2019) 1701–1709, https://doi.org/10.1016/j.ijhydene.2018.11.070.
[49] J. Zhu, L. Hu, P. Zhao, L.Y.S. Lee, K.-Y. Wong, Recent Advances in Electrocatalytic Hydrogen Evolution Using Nanoparticles, Chem. Rev. 120 (2020) 851–918, https://doi.org/10.1021/acs.chemrev.9b00248.
[50] W. Chen, H. Wang, Y. Li, Y. Liu, J. Sun, S. Lee, J.-S. Lee, Y. Cui, Situ Electrochemical Oxidation Tuning of Transition Metal Disulfides to Oxides for Enhanced Water Oxidation, ACS Cent. Sci. 1 (2015) 244–251, https://doi.org/10.1021/acscentsci.5b00227.
[51] Q. Su, P. Wang, Q. Liu, R. Sheng, W. Cheng, J. Ding, Y. Lei, Y. Huang, Dual role of sulfur doping in NiCr LDH for water oxidation: Promoting surface reconfiguration and lattice oxygen oxidation, Appl. Catal. B Environ. Energy 351 (2024) 123994, https://doi.org/10.1016/j.apcatb.2024.123994.
[52] A. Raveendran, M. Chandran, R. Dhanusuraman, A comprehensive review on the electrochemical parameters and recent material development of electrochemical water splitting electrocatalysts, RSC Adv. 13 (2023) 3843–3876, https://doi.org/10.1039/D2RA07642J.
[53] V.D. Silva, T.A. Simões, J.P.F. Grilo, E.S. Medeiros, D.A. Macedo, Impact of the NiO nanostructure morphology on the oxygen evolution reaction catalysis, J. Mater. Sci. 55 (2020) 6648–6659, https://doi.org/10.1007/s10853-020-04481-1.
[54] H.G. Edao, C.-Y. Chang, W.B. Dilebo, F.T. Angerasa, E.A. Moges, Y. Nikodimos, C. B. Guta, K. Lakshmanan, J.-L. Chen, M.-C. Tsai, W.-N. Su, B.J. Hwang, Nickel–Iron Layered Double Hydroxides/Nickel Sulfide Heterostructured Electrocatalysts on Surface-Modified Ti Foam for the Oxygen Evolution Reaction, ACS Appl. Mater. Interfaces 16 (2024) 50602–50613, https://doi.org/10.1021/acsami.4c08215.
[55] Y. Huang, X. Chen, S. Ge, Q. Zhang, X. Zhang, W. Li, Y. Cui, Hierarchical $FeCo_2$ S_4 @CoFe layered double hydroxide on Ni foam as a bifunctional electrocatalyst for overall water splitting, Catal. Sci. Technol. 10 (2020) 1292–1298, https://doi.org/10.1039/C9CY01896D.
[56] J. Wang, B. Zhao, X. Chen, H. Liu, J. Zhang, Immersion-Driven Structural Evolution of NiFeS Nanosheets for Efficient Water Splitting, Nanomaterials 14 (2023) 23, https://doi.org/10.3390/nano14010023.
[57] J. Zhang, R. He, L. Jia, C. You, Y. Zhang, M. Liu, N. Tian, H. Lin, J. Wang, Strategies for Realizing Rechargeable High Volumetric Energy Density Conversion-Based Aluminum–Sulfur Batteries, Adv. Funct. Mater. 33 (2023) 2305674, https://doi.org/10.1002/adfm.202305674.
[58] Y. Gong, Z. Xu, H. Pan, Y. Lin, Z. Yang, X. Du, Hierarchical Ni_3 S_2 nanosheets coated on Co_3 O_4 nanoneedle arrays on 3D nickel foam as an efficient electrocatalyst for the oxygen evolution reaction, J. Mater. Chem. A 6 (2018) 5098–5106, https://doi.org/10.1039/C7TA11104E.
[59] T. Tang, S. Jiao, J. Han, Z. Wang, J. Guan, Partially crystallized Ni–Fe oxyhydroxides promotes oxygen evolution, Int. J. Hydrog. Energy 48 (2023) 5774–5782, https://doi.org/10.1016/j.ijhydene.2022.11.118.
[60] S. Carbone, R.L. Oliveri, B. Patella, G. Aiello, M. Scopelliti, N. Campagna, F. Pellitteri, R. Miceli, A. Affranchi, S. Longo, M. Cellura, P. Mandin, M. Kim, R. Inguanta, Optimized NiFeP alloy for overall water-splitting, Renew. Energy 250 (2025) 123257, https://doi.org/10.1016/j.renene.2025.123257.
[61] A. Affranchi, R.L. Oliveri, S. Longo, G. Miccichè, S. Carbone, F. Bellomo, S. Geraci, B. Patella, N. Moukri, G. Aiello, M. Cellura, P. Mandin, M. Kim, R. Inguanta, Effect of Operating Temperature on Ni–Fe Alloy Nanostructured Electrodes for Alkaline Electrolyzer, ChemElectroChem 12 (2025) e202500042, https://doi.org/10.1002/celc.202500042.
[62] G. Genchev, A. Erbe, Raman Spectroscopy of Mackinawite FeS in Anodic Iron Sulfide Corrosion Products, J. Electrochem. Soc. 163 (2016) C333–C338, https://doi.org/10.1149/2.1151606jes.
[63] J. Deng, Q. Gong, H. Ye, K. Feng, J. Zhou, C. Zha, J. Wu, J. Chen, J. Zhong, Y. Li, Rational Synthesis and Assembly of Ni_3 S_4 Nanorods for Enhanced Electrochemical Sodium-Ion Storage, ACS Nano 12 (2018) 1829–1836, https://doi.org/10.1021/acsnano.7b08625.
[64] W. Li, M. Zhong, X. Chen, S. Ren, S. Yan, C. Wang, X. Lu, Hierarchical amorphous bimetallic sulfide nanosheets supported on Co-C nanofibers to synergistically boost water electrolysis, Sci. China Mater. 66 (2023) 2235–2245, https://doi.org/10.1007/s40843-022-2376-7.
[65] S. Niu, W.-J. Jiang, T. Tang, L.-P. Yuan, H. Luo, J.-S. Hu, Autogenous Growth of Hierarchical NiFe(OH)x/FeS Nanosheet-On-Microsheet Arrays for Synergistically Enhanced High-Output Water Oxidation, Adv. Funct. Mater. 29 (2019) 1902180, https://doi.org/10.1002/adfm.201902180.
[66] J. Chang, G. Wang, Z. Yang, B. Li, Q. Wang, R. Kuliiev, N. Orlovskaya, M. Gu, Y. Du, G. Wang, Y. Yang, Dual-Doping and Synergism toward High-Performance Seawater Electrolysis, Adv. Mater. 33 (2021) 2101425, https://doi.org/10.1002/adma.202101425.
[67] P. Ganesan, A. Sivanantham, S. Shanmugam, Inexpensive electrochemical synthesis of nickel iron sulphides on nickel foam: super active and ultra-durable electrocatalysts for alkaline electrolyte membrane water electrolysis, J. Mater. Chem. A 4 (2016) 16394–16402, https://doi.org/10.1039/C6TA04499A.